*Geophys. J. R. astr. Soc.* (1987) **91**, 461–484

# Observation and modelling of fault-zone fracture seismic anisotropy – I. *P*, *SV* and *SH* travel times

P. C. Leary, Y.-G. Li and K. Aki *Department of Geological Sciences, University of Southern California, Los Angeles, California 90089-0741*

**Summary**. Three-component VSP borehole seismograms taken in the vicinity of an active normal fault in California show strong systematic shear-wave splitting that increases with proximity to the fault. Using Červený's method of characteristics for ray tracing in anisotropic heterogeneous media and Hudson's formulation of elastic constants for media-bearing aligned fractures, we have fitted a suite of *P*, *SV* and *SH* hanging-wall and foot-wall travel times with a simple model of aligned fractures flanking the fault zone. The dominant fracture set is best modelled as parallel to the fault plane and increasing in density with approach to the fault. The increase in fracture density is non-uniform (power law or Gaussian) with respect to distance to the fault. Although the hanging-wall and the foot-wall rock are petrologically the same unit, the fracture halo is more intense and extensive in the hanging wall than in the foot wall. Upon approach to the fault plane, the fracture density or fracture-density gradient becomes too great for the seismic response to be computed by Hudson–Červený procedures (the maximum fracture density that can be modelled is about 0.08). Within this 25 m fracture domain it appears more useful to model the fault and near field fractures as a low-velocity waveguide. We observe production of trapped waves within the confines of the intense fracture interval.

## 1 Introduction

The population, distribution, and particularly the degree of alignment of fractures within a host rock are parameters of increasing geophysical interest. Fracture density, concentration of fractures, and alignment of fractures bear an important relationship to flow magnitude and flow patterns of *in situ* fluids critical to utilization of geothermal and hydrocarbon reservoirs (Long & Witherspoon 1985; Dobecki & Romig 1985; Dyck & Young 1985; Wright *et al.* 1985). Induced seismicity has been connected with hydraulic flow through *in situ* fractures (Zoback & Hickman 1982; Bell & Nur 1978; Simpson 1976). Aligned fractures in geothermal systems (Majer & McEvilly 1979; Aki *et al.* 1982) and in areas of active faulting are primary indicators of current crustal-stress regimes (Zoback, Tsukahara & Hickman

1980). Stephen (1981, 1985) has found seismic anisotropy evidence for relic aligned fractures associated with mid-ocean ridge production. Considerable evidence has been collected recently for large-scale volumes of orientated fracture sets in active tectonic areas in California, Turkey and the USSR (Crampin, Evans & Ucer 1985; Crampin & Booth 1985; Crampin *et al.* 1985; Peacock, Crampin & Fletcher 1987). These fracture systems show some evidence for localized changes in response to local seismic stress drops (Peacock *et al.* 1987; Chen, Booth & Crampin 1987). Finally, evidence for abundant vertical aligned fracture sets in sediments has been recently reported in industry exploration profiling data (Alford 1986; Becker & Perelberg 1986; Lynn & Thomsen 1986; Willis, Rethford & Bielanski 1986).

Fracture density and distribution create velocity inhomogeneties (O'Connell & Budiansky 1974) that can be modelled for *in situ* *P*-wave velocity structure (e.g. Leary & Malin 1982). The degree of fracture alignment manifests itself as seismic velocity anisotropy (Garbin & Knopoff 1973, 1975a,b; Anderson, Minster & Cole 1974; Crampin 1978, 1984; Hudson 1981). While under certain circumstances it is possible to investigate vertical fracture anisotropy with *P*-waves (e.g. Murdock 1980; Kohler & Healy 1981; Leary & Henyey 1985), shear-waves are the natural means of determining the degree of fracture alignment (Crampin 1978, 1984). Shear-wave splitting or birefringence is, to first order, independent of structural heterogeneities that generate seismic velocity direction-dependencies which may be erroneously interpreted as anisotropy. As has been emphasized by Crampin (1978, 1981, 1985), shear-wave splitting signals more than the existence of fracture anisotropy. The degree of shear-wave splitting is a measure of the degree of anisotropy, and the polarization of the split shear-wave components is a direct indicator of the orientation of crack alignment. Additionally, the sensitivity of crack distributions to regional stress makes time-dependent shear-wave polarization observation and interpretation a potential tool in fault-zone monitoring (Evans 1984; Crampin & McGonigle 1981; Crampin, Evans & Atkinson 1984).

While close studies of seismic *P*- and shear-wave anisotropy has been commonly achieved in the laboratory (e.g. Nur 1971; Babuska 1984; Babuska & Pros 1984; Christensen 1984), only recently have the tools become available for systematic observation of *in situ* seismic anisotropy. Three component microseismic arrays in California (Malin & Waller 1985; Peacock *et al.* 1987), Turkey (Crampin & Booth 1985), and USSR (Crampin *et al.* 1985), have recorded numerous instances of shear-wave splitting in seismic radiation from earthquakes. Mobile repeatable shear-wave sources are now in use in conjunction with three-component borehole receivers and with three-component surface arrays (Robertson & Corrigan 1983; Johnson 1986; Majer *et al.* 1987). In some circumstances, e.g. this study, *P*-wave sources create sufficient shear-wave amplitudes for observing shear-wave splitting. In the present report we describe observations of shear-wave propagation over 100–300 m paths in locally intact crystalline rock transected by an active normal fault. The fault zone was presumed to have generated a spatially well-localized, aligned fracture set. The goal of the study was to develop a field method for quantitatively characterizing the fracture-related seismic fabric of a crystalline host rock.

## 2 The experiment

The Cleveland Hill normal fault outcrops in a high-speed ($V_p \simeq 5.8$–$6.0\,\mathrm{km\,s^{-1}}$) metasedimentary stratum on the western flanks of the central Sierran uplift in California (Fig. 1). The fault, dipping 60° to the west, sustained 15 cm of slip during a magnitude 5.7 earthquake in 1975 (Morrison, Stump & Uhrhammer 1976; Lahr *et al.* 1976; Langston & Butler 1976). The rupture aroused considerable interest as the fault was previously unmapped and

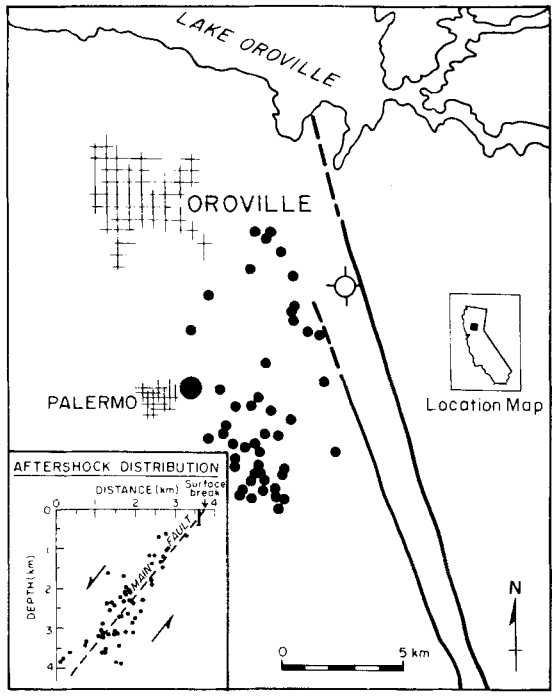


**Figure 1.** Location map for Cleveland Hill fault, Oroville, California, showing epicentres of August 1, 1975 $M = 5.7$ mainshock (large solid circle) and aftershocks (small solid circles). Borehole location denoted by open circle adjacent to the principal fault trace. Inset shows fault plane definition by aftershock hypocentres.

the slip episode occurred within a few years of impounding a major reservoir 15 km from the rupture epicentre (Bell & Nur 1978).

Following the earthquake, the United States Geological Survey drilled a 500 m borehole through the hanging wall into the foot wall. The borehole intersects the fault at a depth of 305 m (Fig. 2). USGS televiewer fracture logs of the borehole reveal the moderate presence of large aperture (1 mm) orientated fractures (Dan Moos private communication). The USGS fracture data show that in the depth interval 220–320 m, crack-face normals are predominantly perpendicular to the fault plane while in the depth interval 120–220 m the crack-face normals are primarily parallel to the fault plane. USGS borehole sonic-velocity log indicates that fracture density increases steadily as the fault zone is approached. We assume that the increasing population of fractures inferred from decreasing sonic velocities are below the resolution of the borehole televiewer.

Using a small, repeatable, mobile, vertical impact-source and a three-component, orientable, 0.5 ms precise borehole seismic-sonde (Leary, Li & Manov 1987), we collected digital seismograms at 12 points in the borehole at depths between 90 and 305 m. At each borehole depth, 20 surface-source offsets were occupied between 60 and 230 m from the borehole. The source points define a line through the borehole in a direction normal to the surface trace of the fault (Fig. 2). Slumping of fault-zone material into the borehole confined our borehole receiver to the upper or hanging-wall 305 m of the hole. The orientation of the sonde at each depth in the borehole was determined by a digital magnetic compass aboard the sonde. Knowledge of the sonde orientation permitted a convenient and secure method of resolving the three-component seismograms into components along specific directions.

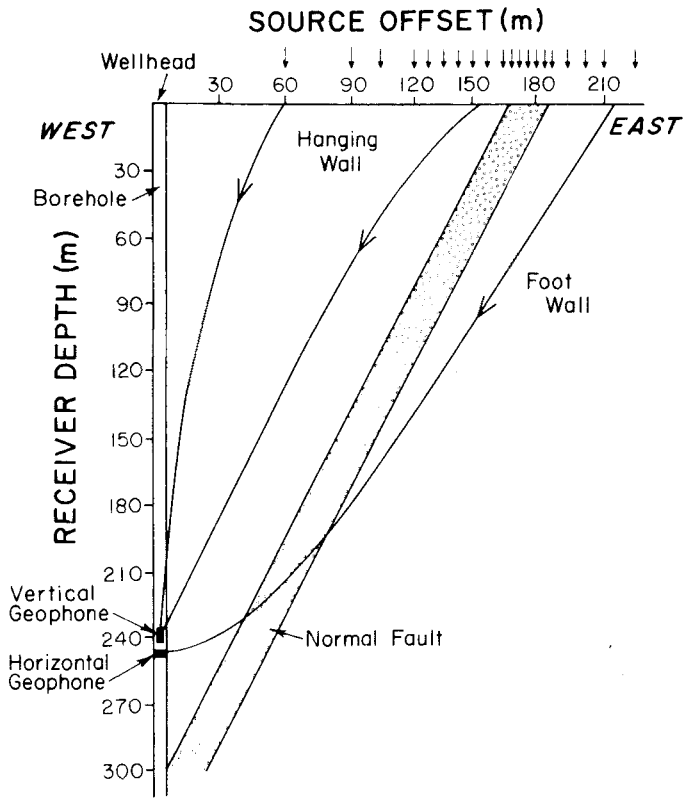


**Figure 2.** Sagittal plane of borehole profile of Oroville fault zone. Source offsets range from 60 to 230 m. Receiver depths range from 90 to 305 m.

The experiment was designed to offer a natural coordinate system of axes with which to describe seismic components of motion in relation to the fault plane. Since the rays are largely parallel to the fault zone (Fig. 2), two reference axes for seismic motion are chosen to be the ray longitudinal and transverse directions within the plane defined by the borehole and line of source points (the sagittal plane); the third reference axis is transverse to the sagittal plane. The selected source offsets and borehole depths provided ray-paths which sampled a full range of potential fracture populations in the hanging wall and, for purposes of contrast, a portion of the foot wall. In particular, source points near the borehole observed by shallow receivers define ray-paths largely avoiding the fault zone, while source offsets distant from the borehole observed at deep receivers define ray-paths restricted to the immediate fault zone environs.

## 3 The observations

Figs 3 and 4 show three-component seismograms from all source offsets at borehole depths of 90, 210 and 290 m. This seismogram arrangement, termed the common receiver format, highlights variations in the properties of the source point. Two amplitude conventions are used for plotting the common receiver seismograms. In order to emphasize the structure within a seismogram Fig. 3 normalizes each component of each seismogram to a fixed plot

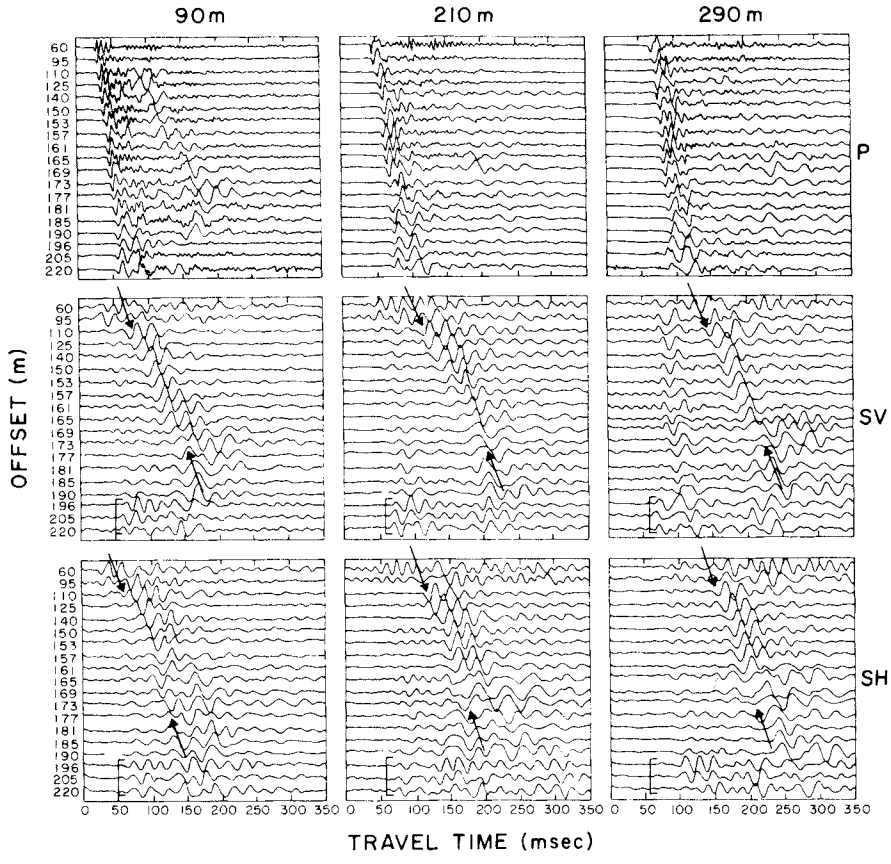


**Figure 3.** Normalized amplitude seismograms at three borehole depths for a range of source offsets. Rows are from top to bottom, *P* (along ray path), *SV* (normal to ray path, in sagittal plane), and *SH* (normal to sagittal plane). Columns are, left to right, depths 90, 210 and 290 m. Note the transition from hanging wall to foot wall marked by early arriving energy at the bottom of each panel (brackets). Note also the clear velocity difference between *SH* and *SV* energy (between opposing arrows) at lower receiver locations.

height. Fig. 4 emphasizes amplitude systematics within the entire suite of seismograms by plotting all components of all seismograms to a single amplitude scale (with the exception that all *P*-wave amplitudes are reduced by a factor of three relative to all shear-wave amplitudes).

The seismograms in Figs 3 and 4 were rotated from raw three-component seismograms into the ray-path dependent coordinate system illustrated in Fig. 2. Using the magnetic orientation of the sonde, a rotation about the vertical axis resolved horizontal motion into components normal to and parallel to the vertical plane of the seismic section (sagittal plane). A second rotation about the horizontal axis normal to the sagittal-plane resolved vertical and in-plane transverse motion into a component along the ray-path and a component normal to the ray-path. For the purpose of resolving the longitudinal component of motion, each ray-path was approximated by the straight line between source and receiver. The sense of motion in the resultant seismograms in Figs 3 and 4 are, from top to bottom, longitudinal motion (along the straight line ray-path), motion perpendicular to the ray-path in the vertical plane, and motion perpendicular to the ray-path in the horizontal plane.

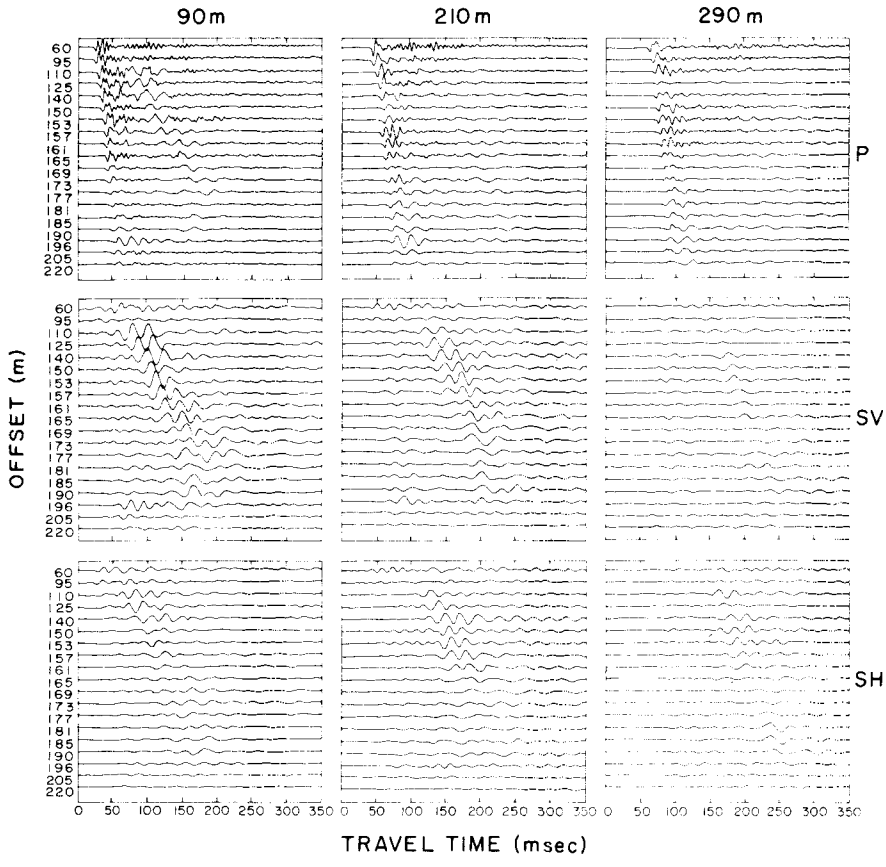


**Figure 4.** Absolute amplitude format for seismograms shown in Fig. 3 (all *P*-wave amplitudes have been scaled down by a factor 3 relative to shear-wave amplitudes). The relative strength of the shear-waves at 210 m compared with 90 m may be due to shear-wave radiation lobes.

Motion in the sagittal plane transverse to the ray-vector will be referred to as *SV* motion while the horizontal motion normal to the sagittal plane will be referred to as *SH* motion. In terms of anisotropy created by fractures parallel to the fault plane *SV* motion is normal to crack faces and *SH* motion is parallel to crack faces. For a fracture set that parallels the fault zone, the *SH* and *SV* motions as we have defined them decouple from one another with the *SH* waves propagating at a greater velocity than the *SV* waves (Hudson 1981; Crampin 1984). Using a common source point display format Fig. 5 compares the suite of *SH* seismograms with the suite of *SV* seismograms for a range of source points. For all source points the *SH* wavelet precedes the *SV* wavelet while the separation interval between *SH* and *SV* wavelets grows as the source point approaches the fault zone. The independent *SH* and *SV* wave travel-time behaviour indicates a population of aligned fractures that parallels the fault zone. These observations accord with USGS televiewer data in the borehole depth interval 220–320 m.

The selected depths of seismograms shown in Figs 3 and 4 range from distances relatively far from the fault zone to distances relatively near the fault zone. The 11 hanging-wall source points span a similar distance range from the fault. Specifically, source offsets less than 110 m may be regarded as far from the fault zone; source offsets in the range of

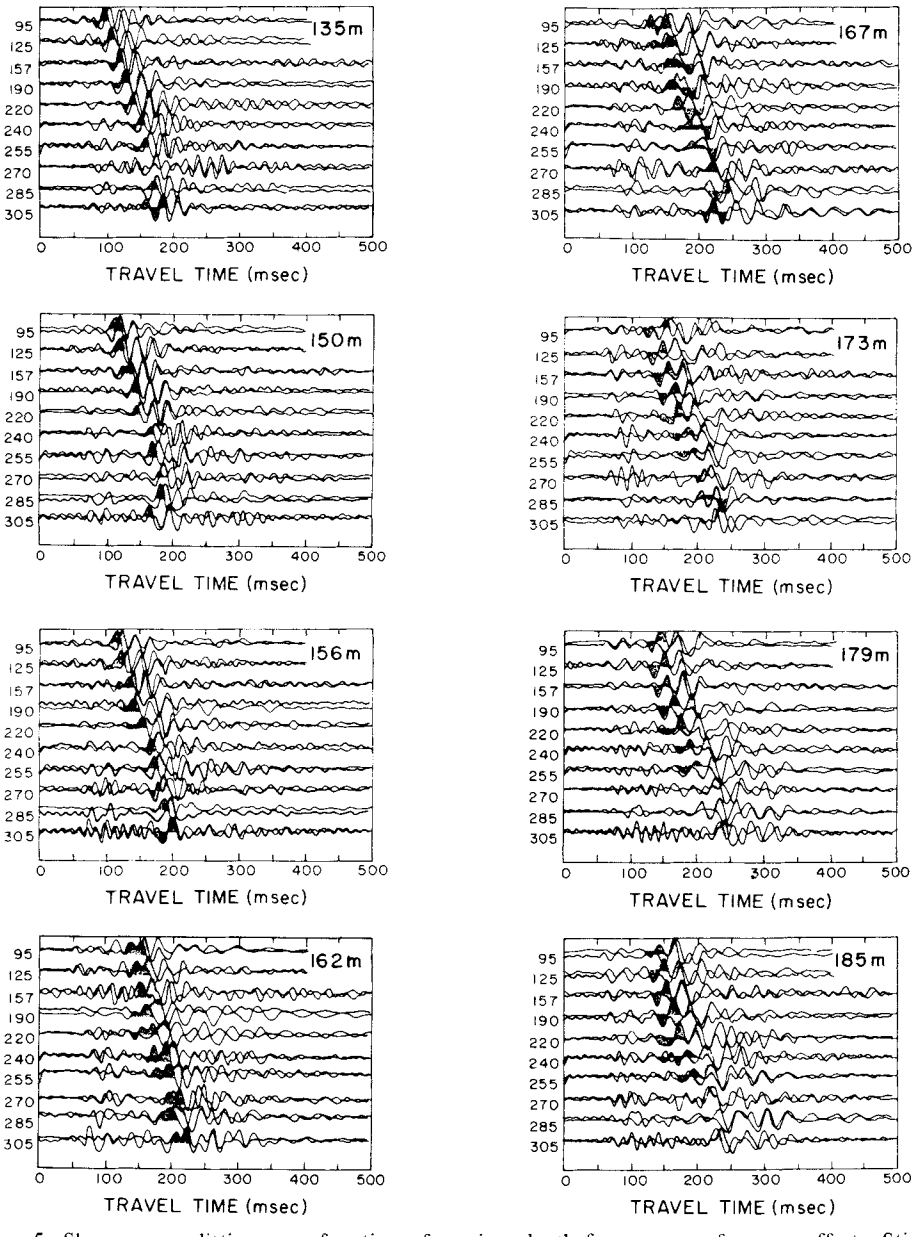


**Figure 5.** Shear-wave splitting as a function of receiver depth for a range of source offsets. Stipling denotes *SH* waves; light shading denotes *SV*. Offset shown in upper right hand corners.

110–135 m are at an intermediate distance, and source offsets between 135 and 165 m are near the fault zone. Source points between 165 and 185 m are within the fault zone; source offsets beyond 185 m are in the foot wall.

The three structural elements of the Cleveland Hills fault zone mechanical system – the hanging wall, the fault zone proper, and the foot wall – may be deduced from an inspection of the seismograms in normalized seismograms in Fig. 3 and the true-amplitude seismograms in Fig. 4. Rays originating in the hanging wall (source offset < 165 m) show a sequence of

strong shear-wave first arrivals indicated by opposing arrows in Fig. 3. Fig. 4 shows the sequence of shear-wave arrivals diminishing in strength as the source point moves toward the fault zone. In the normalized seismograms (Fig. 3) recorded at a depth of 290 m, the lower arrows mark the times at which the *SV* arrivals abruptly develop a lag of 50 ms for source points in the fault zone ($165 \leqslant$ source offset $\leqslant 185$ m). We interpret this discontinuity as marking the fault zone structural element of the fault system. The *SV* and *SH* amplitude systematics of Fig. 4 also indicate a structural change encountered by rays originating at fault zone source points. The discontinuity in *SV*-wave arrivals indicates a cessation of refracted arrivals and the onset of fault zone trapped or guided waves. The characteristic phase properties of the trapped waves are displayed in the common source point format of Fig. 6. For source points beyond the fault zone, the third structural element of the fault system is indicated in Fig. 3 by brackets that mark early arriving horizontal first motions.

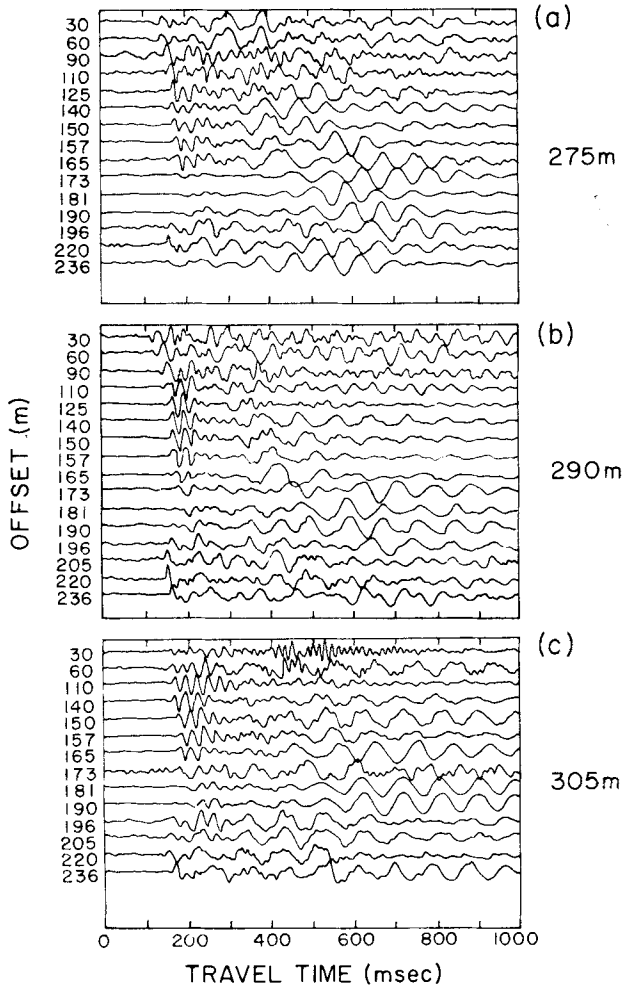


**Figure 6.** Trapped waves in the *SH* (normal to sagittal plane) component for range of offsets observed at three depths, from top to bottom, 275, 290 and 305 m. The long period energy follows the shear-waves, is relatively narrow band and undamped, and possesses either an 0 phase or $\pi$ phase from source point to source point. The standing waves are excited principally at fault-zone offsets (150–190 m), and do not appear at higher receiver positions.

The *P*-wave first motions on the horizontal geophones arise from waves refracted in the foot wall towards the fault zone.

The magnetic orientation of the seismograms in Figs 3–5 is confirmed by noting in Fig. 4 the presence of *P*-motion in the *SV* seismograms and the absence of *P*-motion in the *SH* seismograms. The large amplitude of *SV* motion in the true amplitude seismograms at a depth of 90 m in comparison with *SV* amplitudes at 210 and 290 m depth probably indicates a side lobe of transverse energy generation (e.g. Robertson & Corrigan 1983; Waters 1981). The amplitude of *SV*-motion decays at a faster rate than does the *P*-motion, again suggesting a source effect in which transverse source energy is directed more sideways than downward. Fig. 4 also demonstrates the degree with which *SH* motion at the Cleveland Hills fault is generated by the vertical impact source. Observing that *SV* and *SH* amplitudes decay at different rates as a function of receiver depth, and noting from Fig. 5 that *SV* and *SH* travel times differ systematically with depth, we infer that *SH* motion is generated by anisotropy or heterogeneity at the source rather than along the ray-path. The constant phase of the *SH* wave probably reflects a local gradient in heterogeneity or anisotropy in the rock which couples *SH* motion to *P–SV* motion in a unique sense for all source points.

The velocity of the seismic shear-waves in Figs 3–5 is slow in comparison with the *P*-waves. For $V_p \sim 5.5\ \mathrm{km\,s^{-1}}$ and $V_s \sim 2.2\ \mathrm{km\,s^{-1}}$, we may derive an isotropic Poisson's ratio

$$\nu \equiv \tfrac{1}{2}\frac{(V_p/V_s)^2 - 2}{(V_p/V_s)^2 - 1} \sim 0.40$$

indicating that in the vicinity of the fault zone the medium has substantial compressive strength and reduced shear strength. We have noted that the predominant orientation of cracks identified in the borehole televiewer images between 200 and 300 m is parallel to the fault and have speculated that the population of cracks smaller than instrumental resolution behaves similarly. We note here that the conclusion is strengthened by the large ratios of *P*-wave to shear-wave velocities; the *P*-wave plane wave elastic modulus parallel to crack faces can be stiff despite a small elastic modulus of rigidity controlling shear-wave velocities. We conclude that there is strong observational evidence for fracture induced seismic anisotropy in the vicinity of the Cleveland Hill fault.

## 4 *P–SV–SH* seismic travel times in a heterogeneous anisotropic medium of plane parallel fractures

In order to quantify the structural inferences made from the borehole seismograms shown in Figs 3–5 and to obtain a physical measure of the fracture population in the vicinity of the fault, we have implemented the Červený & Pšenčík (1972) 2-D ray tracing procedure for heterogeneous anisotropic media with a model for elastic constants of a medium containing aligned fractures. The suite of borehole seismograms provides several hundred *P*-, *SV*-, and *SH*-travel times with which to constrain a seismic structural model of the fault system.

The physical model for the seismic anisotropy of a medium bearing aligned fractures is Hudson's (1981) presentation of the original Garbin & Knopoff (1973, 1975a, b) treatment. A seismic model of either the hanging wall or the foot wall may be specified by as few as four parameters: the isotropic ambient host-rock *P*-wave velocity $V_{p_0}^2 = (\lambda_0 + 2\mu_0)/\rho$; the host medium shear-wave velocity $V_{s_0}^2 = \mu_0/\rho$; the aligned fracture density $e$; and the aligned fracture orientation relative to the fault plane. First-order observation at Oroville gives strong constraints on the whole rock velocities, $V_{p_0}$ and $V_{s_0}$. Assuming a nominal density of $2.5\ \mathrm{g\,cm^{-3}}$ consistent with metasedimentary rock, we obtain the host-rock isotropic elastic

constants $\lambda_0$ and $\mu_0$. Primary observation of *SH–SV* velocity differentials has indicated that the fractures are aligned predominantly parallel to the fault plane. We start our modelling with this assumption. The free model parameter is the crack density $e$, which may be permitted to vary with distance from the fault plane according to simple parameterized functional forms.

A remaining physical characterization of the seismic model is the degree of fluid saturation of the fractures. A small population of thin, fluid-saturated fractures greatly reduces the effect of fractures on the compressive modulus of the rock while not altering the role of cracks in reducing the rigidity modulus (e.g. Crampin 1984). The water table at Oroville is sufficiently shallow to suggest that the crack voids are fluid filled. However, if the water has any void space in which to displace during the passage of a plane wave at seismic frequencies, the possibility of unsaturated cracks must be admitted (O'Connell & Budiansky 1977). However, for the present experiment, evidence indicates that the majority of *P*- and

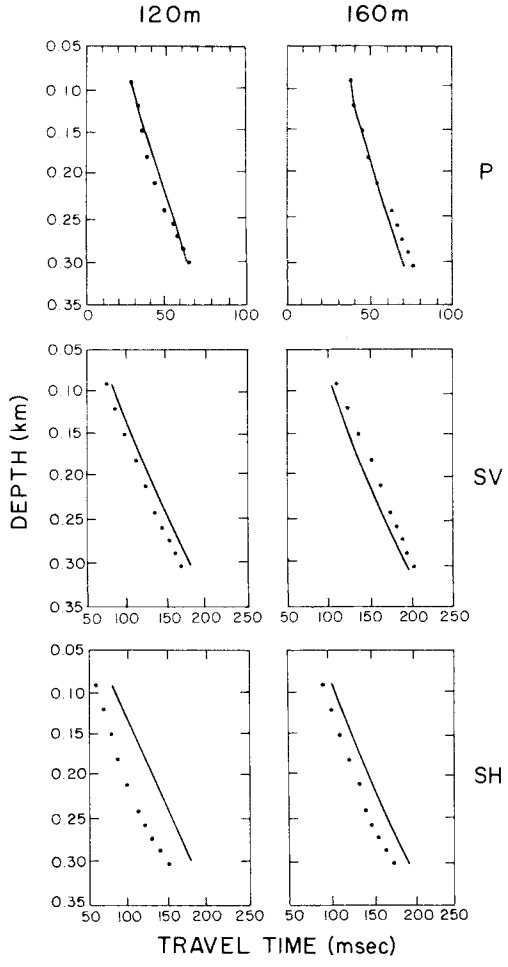


**Figure 7.** Runge–Kutta integrated travel times for Červený ray tracing algorithm for a homogeneous, isotropic medium. Left column, source offset 120 m; right column, source offset 160 m. While *P*-travel times do not disagree greatly with approach to the fault zone, shear-wave travel times fit poorly to the homogeneous isotropic model.

shear-wave travel paths are parallel to the face of the predominant fracture set. For this orientation of wave propagation, it is not easy to distinguish between wet and dry *P*-wave velocities (e.g. Crampin 1984). Consequently we do not expect to be able to decide effectively whether the fractures are saturated (wet) or unsaturated (dry). We do not introduce this parameter into our model, although we discuss below secondary evidence for a substantial degree of fracture saturation at Oroville.

The principal unknown quantities in our model of the Cleveland Hill fault system are the density and distribution of fractures in the fracture halo on either side of the fault zone proper, and the fracture density in the fault zone proper. To specify the crack density $e(\zeta)$ we adopt a range of functional forms that depend on $\zeta$, the distance normal to the fault plane. We ignore possible variation of $e(\zeta)$ with distance $\xi$ along the fault plane (such variation could originate in crack closure with increasing confining pressure with depth $z$). The structural inhomogeneity is assumed to be planar and parallel to the fault. The fault

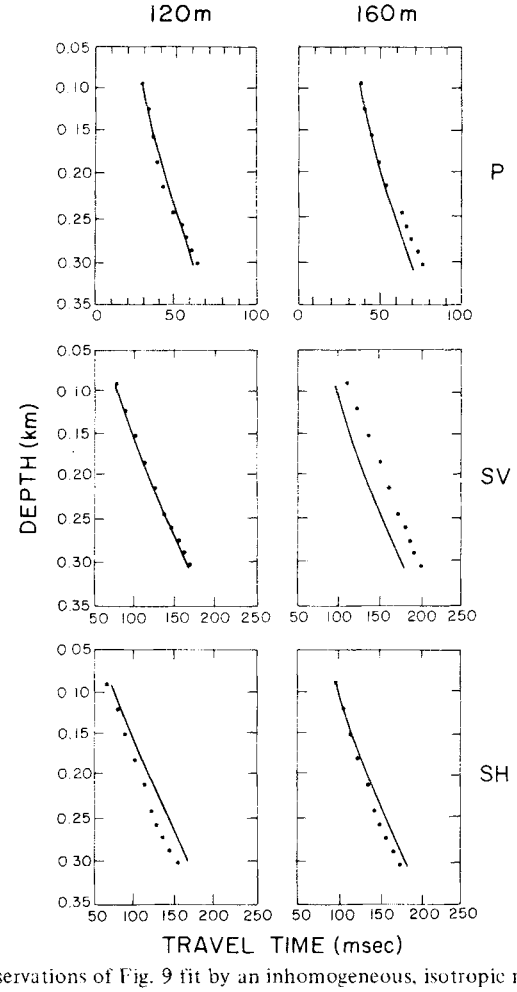


**Figure 8.** Travel-time observations of Fig. 9 fit by an inhomogeneous, isotropic model of elastic constants. The fit improves over the homogeneous isotropic model, clearly indicating a heterogeneous medium; but *SV* behaviour is markedly different from *SH* behaviour.

zone proper is assumed to be a constant width zone of intense fracturing. The simplest model of crack density inhomogeneity is a linear form $e(\zeta) = e_0 + e_1(\zeta_0 - \zeta)$ corresponding to the first term of a Taylor series expansion of a non-uniform crack population. The distance parameter $\zeta$ is defined as the interval between the fault plane and the distance $\zeta_0$ at which the cracks population diminishes to a background value $e_0$. The product $e_1 * \zeta_0$ is the fracture density at the edge of the fault zone proper. For a constant gradient distribution of fracture density in the fracture halo the fault zone proper appears as an abrupt change in crack density and seismic velocity. If the hanging- or foot-wall fracture density increases non-linearly with approach to the fault plane, we may use a power law description, $e(\zeta) = e_0 + e_1(\zeta_0 - \zeta)^\alpha$, where again $\zeta_0$ denotes the scale length of the fracture domain and $e_0$ denotes a background crack density; $e_1 * \zeta_0^\alpha$ now gives the fracture density at the fault zone proper. If the hanging or foot wall crack population is non-linear but effectively continuous at the fault zone, we may wish to attempt to describe both the fracture halo and the fault-zone fracture density by a single formula. Accordingly we use as a model crack density the Gaussian form $e(\zeta) = e_0 \exp[-(\zeta - \zeta_0)^2/\zeta_c^2]$, where $e_0$ here is the maximum crack density and $\zeta_c$ is a scale factor for the distance between the fault zone centre $\zeta_0$ and the length variable $\zeta$.

For a variety of test assumptions about the fault-zone hanging-wall and foot-wall fracture structure we have obtained operator-ascertained 'best fits' to the suite of *P*, *SV* and *SH* travel-time curves for a range of source points (100–165 m for the hanging wall; 185–230 m for the foot wall). Details of the ray tracing procedure may be seen in three appendices. Assumptions about the fracture structure that we tested comprise (i) absence of fractures (isotropic homogeneous medium), (ii) absence of aligned fractures (an isotropic inhomo-

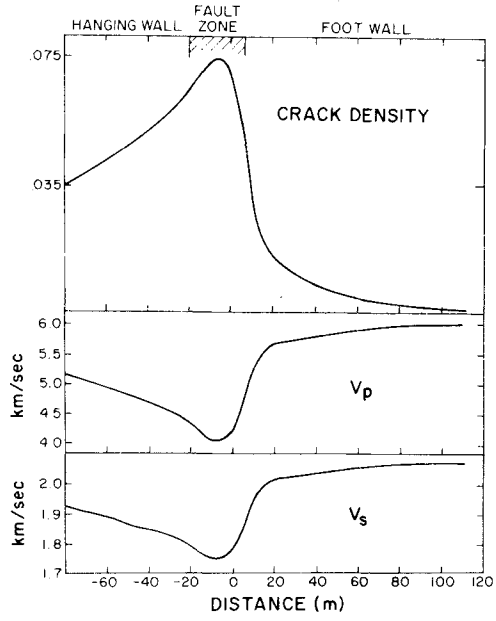


**Figure 9.** Top: best fit crack distribution. The distribution is a cubic spline-smoothed curve comprising separate constant gradient crack density distributions for hanging and foot wall joined to a Gaussian density distribution centred on the fault-zone centre. The optimized distribution parameters are given in Table 1. Bottom: *P* and *SV* velocities due to above fracture distribution, for rays parallel to fault plane.

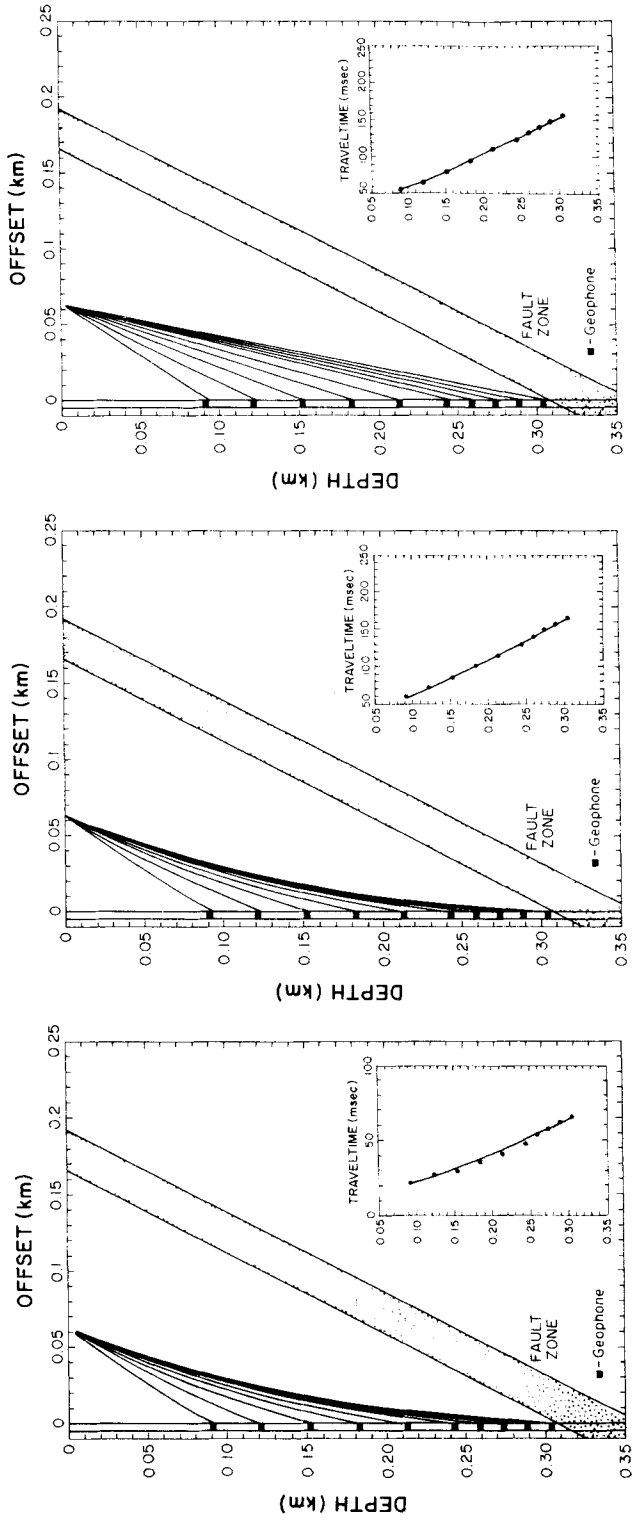


**Figure 10.** Best-fit travel times for source offset 60 m.

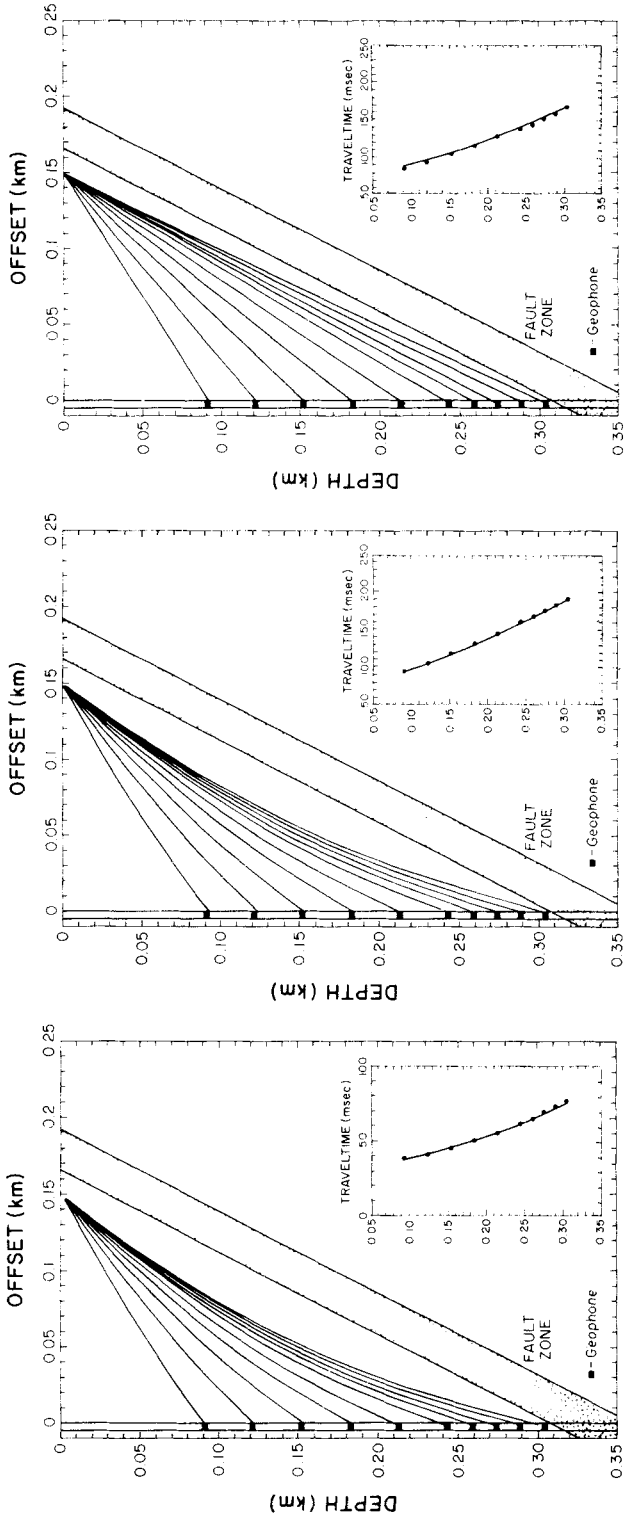


**Figure 11.** Best-fit travel times for source offset 160 m.

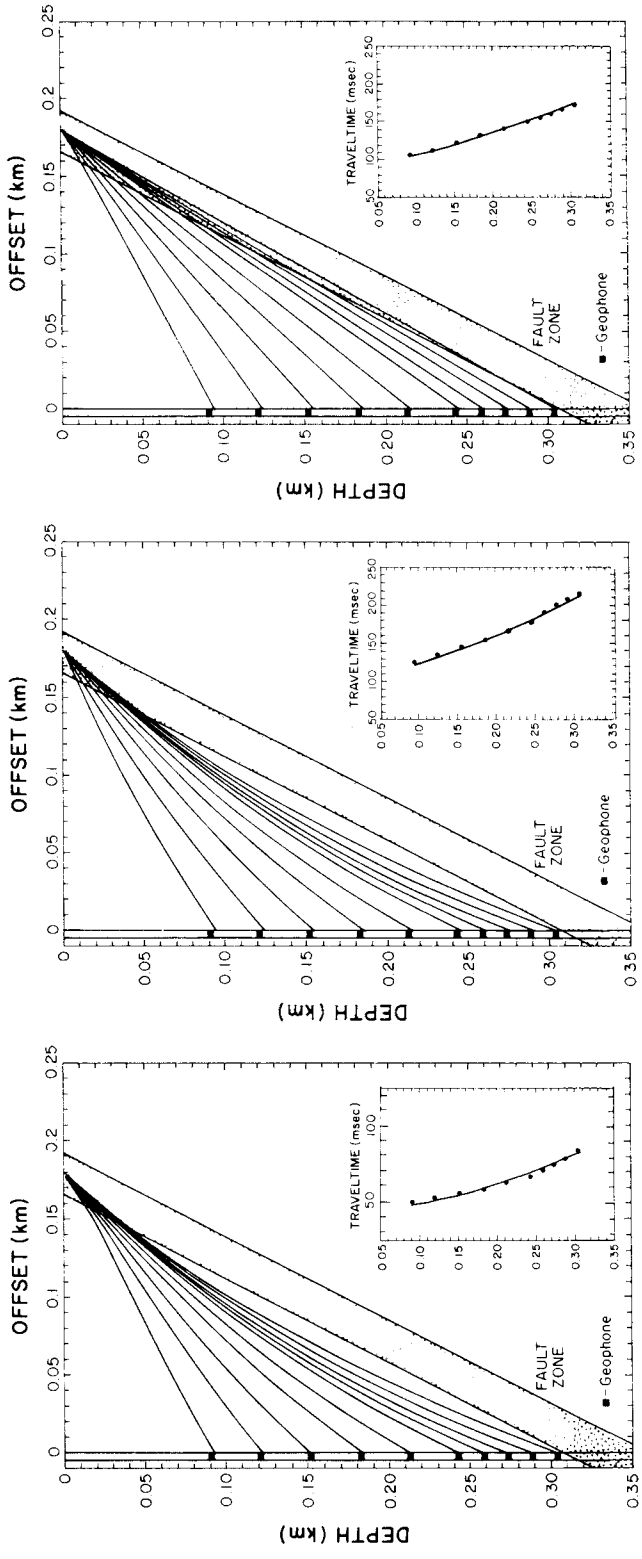


**Figure 12.** Best-fit travel times for source offset 180 m.

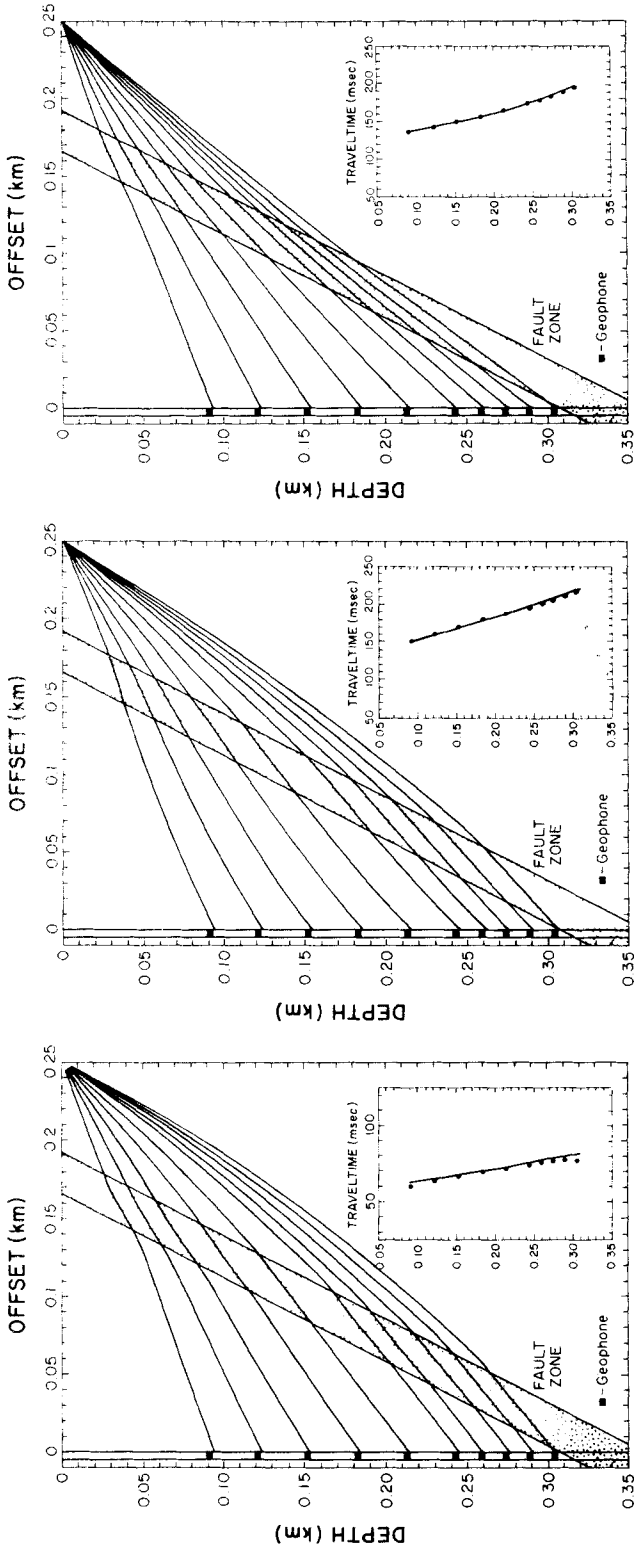


**Figure 13.** Best-fit travel times for source offset 250 m.

geneous medium with inhomogeneity normal to the fault zone), (iii) aligned uniform fractures (homogeneous transversely anisotropic medium), and (iv) aligned non-uniform fractures (inhomogeneous, transversely isotropic media). In category (iv), we tested three fracture distributions, (iv-a) linear, (iv-b) power law, and (iv-c) Gaussian. The aligned fractures of the anisotropic models have been assumed on the basis of Fig. 5 to be predominantly parallel to the fault zone. The fitting procedure is to obtain a best-fit fracture density parameterization for one component of particle motion, usually the *P*-component, and to then compute the prescribed travel-time curves for the remaining two components.

Figs 7 and 8 indicate that the model catagories (i) and (ii) yield unsatisfactory travel-time curves for all components of motion in the hanging wall. In each category, at least one component of motion is badly fit by the model. More comprehensive agreement with the observed *P*-, *SV*- and *SH*-travel times is afforded by the class of heterogeneous, transversely isotropic models. Among these models, the two non-linear crack distributions produce superior fits to that produced by the linear distribution, with the power-law fracture distribution slightly more in agreement with observation than the Gaussian distribution.

To model the entire fault system (hanging wall–fault zone proper–foot wall), we simplified the parameters by using constant crack density gradients for the hanging and footwalls and joined them by cubic splines to a symmetric Gaussian fracture distribution in the fault zone proper. The spline procedure was necessary to keep the gradient terms within tolerable numerical bounds (see Appendices B and C) and effectively absorbed the power law behaviour of the fracture density near the fault zone. We then adjusted the gradient and Gaussian parameters to produce a model travel-time dataset for all surface source points to all receivers for the *P*-, *SV*- and *SH*-components of motion. Fig. 9 shows the final model crack distribution and the *P*–*SV* velocity distribution for rays travelling parallel to the fault plane. Table 1 gives the parameters of the fracture distribution. Figs 10–13 show selected travel paths and travel-time fits derived from the Fig. 9 fracture distribution.

**Table 1.** Fracture distribution model parameters.

| | *M*1 | *M*2 | *M*3 | *M*4 | *M*5 | *M*6 | *M*7 | *M*8 | Rms |
|---|---|---|---|---|---|---|---|---|---|
| Forward fit | 0.072 | 0.45 | 0.3 | 4.25 | 26 | 30 | 0.17 | 0.19 | 2.68 |
| Inverse fit | 0.076 | 0.47 | 0.28 | 4.30 | 27.5 | 30 | 0.165 | 0.19 | 0.75 |

*M*1 Maximum crack density in fault zone (dimensionless).
*M*2 Crack density gradient, hanging wall ($km^{-1}$).
*M*3 Crack density gradient, footwall ($km^{-1}$).
*M*4 Rigidity/density of host rock ($km\ s^{-2}$).
*M*5 Compressibility/density of host rock ($km\ s^{-2}$).
*M*6 Fault zone crack density Gaussian shape factor (dimensionless).
*M*7 Boundary of fault zone against hanging wall (km).
*M*8 Boundary of fault zone against foot wall (km).

The top row of parameters in Table 1 lists best-fit values as determined with a forward procedure by the trial and error method. These parameters were used to define the starting point for an optimization procedure (Aki, Christoffersson & Husebye 1977) that produced the final parameter selection labelled 'Inverse' in Table 1. The optimization procedure reduced the rms travel-time fitting error for 520 points to less than 1 ms $point^{-1}$ from the initial forward parameter best-fit rms residual of 2–3 ms $point^{-1}$. The change in parameter values effected by the optimization procedure never exceeds 10 per cent of the initial parameter value. The change in parameter values serves as an upper bound on the accuracy of the parameter estimates.

## 5 Discussion

Among the inhomogeneous transversely isotropic models, the principal distinction between the fits lies in the *SV* travel-time curve. The travel-time plots favour a steeper than linear increase in crack density. The high density of cracks near the fault zone refracts *SV* rays away from the fault zone, creating the *SV* delays relative to the *SH* times shown in Figs 10–13. This behaviour may be further examined by inspecting the perturbation elastic terms given by Hudson for *SH* and *SV* waves travelling along the fracture face (see Appendices A and B). For *SH* waves one of Hudson's perturbation terms is zero where the second term, while proportional to the fracture density, is of lesser importance because it affects only the small $q$ component of the ray vector; the large component $p$ remains constant. As a result, the effect of fracture density on *SH* is relatively small, permitting the *SH* wave close access to the fault (Figs 10–13). In contrast, the fracture density for the *SV* polarization involves four elastic parameters, $A_{11}$, $A_{33}$, $A_{13}$ and $A_{55}$ and both components $(p, q)$ of the ray parameter. In these circumstances, the increasing fracture density forces the *SV*-wave away from the fault zone.

The best fitting model of the seismic response of the hanging wall is the power law increase in aligned crack density. This model, as well as the Gaussian and linear distributions of fracture density, fails most noticeably for the *SV* component of motion with source points within the fault zone. The models cannot completely account for the delay observed in the *SV* arrivals. The *SV* delays increase as the source moves further on to the surface trace fault zone. The model discrepancy may indicate failure of the Hudson–Červený assumptions of dilute fracture densities and/or small fracture-density gradients. The model density of fracture and fracture gradient at the source point 162 m from the wellhead is 7 per cent. The range of validity of the models is briefly discussed in Appendix C.

A number of considerations have been omitted from the model. We have ignored structural heterogeneity for which evidence exists both inside and outside the suite of seismograms shown in Fig. 3. We have assumed that all heterogeneity can be traced to fractures aligned parallel to the fault. No population density of randomly aligned fractures has been assumed. We have ignored vertical fracture sets and vertical fracture gradients. The model does not try to distinguish between wet and dry fractures. The systematics of seismogram amplitudes and of $Q$ has not been attempted, although Gajewski & Pšenčík (1987) have developed Červený-based procedures for synthetic seismograms.

In part these deficiencies are caused by insufficient observation. To effectively model wet and dry fracture components it would be pertinent to obtain *P*-wave travel times normal to the fault plane. To test for a population of random fractures and/or vertical fractures requires more careful observation of the hanging wall and foot wall away from the fault. The question of seismic amplitudes and $Q$ probably requires control for the seismic radiation pattern of the impact source in an anisotropic medium and control for the existence of lateral heterogeneity.

The values of the host rock model elastic constants, $\lambda_0 \cong 687$ kbar and $\mu \cong 110$ kbar, derived from Table 1 are themselves indicative of a highly fractured rock. As there is little evidence for fracture-related anisotropy in the host rock, the fracture theory of elastic constants given by O'Connell & Budiansky (1974) for unaligned cracks is appropriate. O'Connell & Budiansky show that rocks with a large bulk modulus and a reduced rigidity modulus are associated with immobile fracture fluids. The conclusions that the host rock adjacent to the Cleveland Hill fault is saturated with fluids suggests that our formulation of the aligned fracture system (Appendix A) requires modification to allow for trapped fluids. Specifically the constant $U_{33}$ of Appendix A will be reduced due to the incompressibility of

interstitial fluid (Hudson 1981; Crampin 1984). Adjustment of $U_{33}$ will in turn affect the estimate of the host rock parameter $\lambda_0$. However, as remarked, careful observation of *S*- and *P*-wave propagation normal to the fault plane is necessary for quantitative characterization of the fluid content of the host rock and its aligned fracture system.

## 6 Conclusions

We have presented a simple quantitative analysis of the observed response of the hanging and foot walls of an active normal fault. The rock in the vicinity of the fault appears to be fundamentally anisotropic, probably due to a population of fractures dominantly aligned parallel to the fault. We believe we can eliminate from consideration seismic models of the hanging and foot walls that are neither inhomogeneous nor anisotropic. The closest fitting seismic model is that of an isotropically fractured host medium that bears a population of aligned fractures whose density increases non-linearly with approach to the fault zone. At some point the fracture density and/or fracture density gradient appears to exceed the validity of our ray theoretical procedure for *SV* travel-time computation. At this point we may wish to regard the fault zone as a low velocity layer rather than a refracting medium.

The borehole seismic study of the active normal Cleveland Hill fault system at Oroville, CA, establishes a number of features which may have wider applications:

(1) Systems of naturally aligned fractures exist adjacent to faults.

(2) Such fracture systems can be investigated by three-component borehole seismometry with ±1 ms or better resolution of shear-wave splitting and travel-time modelling.

(3) Surface impact sources may generate sufficient shear-wave energy of all polarizations to conduct a three-component investigation.

(4) Available physical descriptions (e.g. Hudson 1981) of an elastic aligned fracture medium appear adequate to produce quantitative seismic travel-time models of a fracture dominated refractor in terms of a reasonable fracture distribution, provided the fracture population is not too dense ($e \leqslant 0.08$).

(5) The ray-tracing procedure of Červený and co-workers is suitable, at least for travel-time computations, at wavelengths comparable to the physical dimension of the system investigated, provided the fracture gradients are not too great ($e_1 \leqslant 0.003\ \mathrm{m}^{-1}$).

(6) If fracture inhomogeneity becomes too intense to be treated as part of a refraction system, the intense fracture system may possibly be isolated as a low-velocity channel and investigated by methods appropriate to trapped waves.

## Acknowledgments

We are grateful to Dan Moos and Mark Zoback for conversations and for access to unpublished USGS data from the Oroville borehole. Our observations were discussed on numerous occasions with Stuart Crampin and our modelling procedure with Ivan Pšenčík and Vladimir Červený. Mr J. W. Rutherford, on whose property the Oroville borehole is located, granted us repeated and ready access for conduct of the borehole surveys. Field work was supported by USGS Contract No. 14-08-0001-21274, NSF Grant EAR-8213145 and DOE Contract No. DE-FG03-85ER13336. D. V. Manov and J. L. Scott completed the VSP crew. Sue Turnbow, Desser Monton and Janet Dodds prepared the manuscript.

## References

Aki, K., Christoffersson, A. & Husebye, E. S., 1977. Determination of the three-dimensional seismic structure of the lithosphere, *J. geophys. Res.*, **82**, 277–296.

Aki, K., Fehler, M., Aamodt, R. L., Albright, J. N., Potter, R. M., Pearson, C. M. & Tester, J. W., 1982. Interpretation of seismic data from hydraulic fracturing experiments at Fenton Hill, N.M., hot dry rock geothermal site, *J. geophys. Res.*, **87**, 936–944.

Alford, R. M., 1986. Shear data in the presence of azimuthal anisotropy: Dilley, TX (expanded abstract), *56th Annual int. SEG meeting, Houston.*

Anderson, D. L., Minster, B. & Cole, D., 1974. The effect of oriented cracks on seismic velocities, *J. geophys. Res.*, **79**, 4011–4015.

Babuska, V., 1984. *P*-wave velocity anisotropy in crystalline rocks, *Geophys. J. R. astr. Soc.*, **76**, 113–120.

Babuska, V. & Pros, Z., 1984. Velocity anisotropy in grandiorite and quartzite due to the distribution of microcracks, *Geophys. J. R. astr. Soc.*, **76**, 121–128.

Becker, D. F. & Perelberg, A. I., 1986. Seismic detection of sub-surface fractures (expanded abstract), *56th Annual Int. SEG meeting, Houston.*

Bell, M. L. & Nur, A., 1978. Strength changes due to reservoir-induced pore pressure and stresses and applications to Lake Oroville, *J. geophys. Res.*, **83**, 4469–4483.

Beyer, W. H., 1984. *CRC Standard Mathematical Tables*, 27th edn, CRC Press.

Červený, V., 1972. Seismic rays and ray intensities in inhomogeneous anisotropic media, *Geophys. J. R. astr. Soc.*, **29**, 1–13.

Červený, V. & Pšenčík, I., 1972. Rays and travel time curves in inhomogeneous, anisotropic media, *Z. Geophysik*, **38**, 565–577.

Červený, V. & Firbas, P., 1984. Numerical modelling and inversion of travel times of seismic body waves in inhomogeneous anisotropic media, *Geophys. J. R. astr. Soc.*, **76**, 41–52.

Chen, T. C., Booth, D. C. & Crampin, S., 1987. Shear-wave polarizations near the North Anatolian fault – III. Observations of temporal changes, *Geophys. J. R. astr. Soc.*, **91**, 287–311.

Christensen, N. I., 1984. The magnitude, symmetry and origin of upper mantle anisotropy based on fabric analysis of ultramafic tectonites, *Geophys. J. R. astr. Soc.*, **76**, 89–112.

Crampin, S., 1978. Seismic wave propagation through a cracked solid: polarization as a possible dilatancy diagnostic, *Geophys. J. R. astr. Soc.*, **53**, 467–496.

Crampin, S., 1981. A review of wave motion in anisotropic and cracked elastic media, *Wave Motion*, **3**, 343–391.

Crampin, S., 1984. Effective anisotropic elastic constants for wave propagation through cracked solids, *Geophys. J. R. astr. Soc.*, **76**, 135–145.

Crampin, S., 1985. Evaluation of anisotropy by shear wave splitting, *Geophysics*, **50**, 142–152.

Crampin, S. & McGonigle, R., 1981. The variation of delays in stress-induced polarization anomalies, *Geophys. J. R. astr. Soc.*, **64**, 115–131.

Crampin, S. & Booth, D. C., 1985. Shear-wave polarization near the North Anatolian Fault; interpretation in terms of crack-induced anisotropy, *Geophys. J. R. astr. Soc.*, **83**, 75–92.

Crampin, J., Evans, R. & Atkinson, B. K., 1984. Earthquake prediction: a new physical basis, *Geophys. J. R. astr. Soc.*, **76**, 147–156.

Crampin, S., Evans, R. & Üçer, S. B., 1985. Analysis of records of local earthquakes: the Turkish Dilatancy Projects, *Geophys. J. R. astr. Soc.*, **83**, 1–16.

Crampin, S., Booth, D. C., Krasnova, M. A., Chesnokov, E. M., Maximov, A. B. & Tarasov, N. T., 1985. Shear-wave polarizations in the Peter First Range indicating crack-induced anisotropy in a thrust-fault regime, *Geophys. J. R. astr. Soc.*, **84**, 401–412.

Dobecki, T. L. & Romig, P. R., 1986. Geotechnical and groundwater geophysics, *Geophysics*, **50**, 2621–2636.

Dyck, A. V. & Young, R. P., 1985. Physical characterization of rock masses using borehole methods, *Geophysics*, **50**, 2530–2541.

Evans, R., 1984. Anisotropy, a pervasive feature of fault zones?, *Geophys. J. R. astr. Soc.*, **76**, 157–164.

Garbin, H. D. & Knopoff, L., 1973. The compressional modulus of a material permeated by a random distribution of free circular cracks, *Q. appl. Math.*, **30**, 453–464.

Garbin, H. D. & Knopoff, L., 1975a. The shear modulus of a material permeated by a random distribution of free circular cracks, *Q. appl. Math.*, **33**, 296–300.

Garbin, H. D. & Knopoff, L., 1975b. Elastic moduli of a medium with liquid-filled cracks, *Q. appl. Math.*, **33**, 301–303.

Gajewski, D. & Pšenčík, I., 1988. Computation of high-frequency seismic wavefields in 3-D laterally inhomogeneous anisotropic media, *Geophys. J. R. astr. Soc.*, **91**, 383–411.

Hudson, J. A., 1981. Wave speeds and attenuation of elastic waves in material containing cracks, *Geophys. J. R. astr. Soc.*, **64**, 133–150.

Johnson, D. H., 1986. VSP detection of fracture-induced velocity anisotropy (expanded abstract), *56th Annual Int. SEG meeting, Houston.*

Kohler, W. M. & Healy, J. H., 1981. The mechanisms of anisotropic wave velocity in crystalline rocks of the Mojave Desert (abstract), *Eos. Trans. Am. geophys. Un.*, **62**, 961.

Lahr, K. M., Lahr, T. C., Lindh, A. G., Bufe, C. G. & Lester, F. W., 1976. The August 1978 Oroville earthquakes, *Bull. seism. Soc. Am.*, **66**, 1088–1100.

Langston, C. A. & Butler, R., 1976. Focal mechanism of the August 1, 1975 Oroville earthquake, *Bull. seism. Soc. Am.*, **66**, 111–1120.

Leary, P. C. & Malin, P. E., 1982. Millisecond accurate monitoring of seismic travel times over 13- and 18-kilometer baselines, *J. geophys. Res.*, **87**, 6919–6930.

Leary, P. C. & Henyey, T. L., 1985. Anisotropy and fracture zones about a geothermal well from *P*-wave velocity profiles, *Geophysics*, **50**, 25–36.

Leary, P. C., Li, Y.-G. & Manov, D. V., 1987. A microprocessor-based borehole seismic sonde, *Geophysics*, to appear.

Long, J. C. S. & Witherspoon, P. A., 1985. The relationship of the degree of interconnection to permeability in fracture networks, *J. geophys. Res.*, **90**, 3087–3098.

Lynn, H. B. & Thomsen, L. A., 1986. Reflection shear-wave data along the principal axes of azimuthal anisotropy (expanded abstract), *56th Annual Int. SEG meeting, Houston.*

Majer, E. L & McEvilly, T. V., 1979. Seismological investigations at the Geysers geothermal field, *Geophysics*, **44**, 246–269.

Majer, E. L., McEvilly, T. V., Eastwood, F. S. & Myer, L. R., 1987. Fracture detection using *P*- and shear-wave VSPs at the Geysers geothermal field, *Geophysics*, to appear.

Malin, P. E. & Waller, J. A., 1985. Preliminary results from vertical seismic profiling of Oroville, CA, microearthquake shear-waves, *Geophys. Res. Lett.*, 137–140.

Morrison, P. W., Stump, B. W. & Uhrhammer, R., 1976. The Oroville earthquake sequence of August, 1975, *Bull. seism. Soc. Am.*, **66**, 1065-1084.

Murdock, J. N., 1980. Seismic velocity structure of the metamorphic belt of central California, *Bull. seism. Soc. Am.*, **70**, 203–221.

Nur, A., 1971. Effects of stress on velocity anisotropy in rocks with cracks, *J. geophys. Res.*, **76**, 2022.

O'Connell, R. J. & Budiansky, B., 1974. Seismic velocities in dry and saturated cracked solids, *J. geophys. Res.*, **79**, 5412.

O'Connell, R. J. & Budiansky, B., 1977. Viscoelastic properties of fluid-saturated cracked solids, *J Res.*, **82**, 5719.

Peacock, S., Crampin, S. & Fletcher, J. B., 1987. Shear-wave polarizations in the Anza seismic gap southern California: temporal variations as possible precursors, *J. geophys. Res.*, in press.

Robertson, J. D. & Corrigan, D., 1983. Radiation studies on a shear-wave vibrator in near-surface shale, *Geophysics*, **48**, 19–26.

Simpson, D. W., 1976. Seismicity changes associated with reservoir loading, *Eng. Geol.*, **10**, 123–150.

Stephen, R. A., 1981. Seismic anisotropy observed in upper oceanic crust, *Geophys. Res. Lett.*, **8**, 865–868.

Stephen, R. A., 1985. Seismic anisotropy in the upper oceanic crust, *J. geophys. Res.*, **90**, 11393–11396.

Waters, K. H., 1981. *Reflection Seismology*, John Wiley and Sons, Chichester.

Willis, H. A., Rethford, G. L. & Bielanski, E., 1986. Azimuthal anisotropy; occurrence and effect on shear wave data quality, *56th Annual Int. SEG meeting, Houston.*

Wright, P. M., Ward, S. H., Ross, H. P. & West, R. C., 1985. State-of-the-art geophysical exploration for geothermal resources, *Geophysics*, **50**, 2666–2699.

Zoback, M. D. & Hickman, S., 1982. *In situ* study of physical mechanisms controlling induced seismicity at Monticello Reservoir, South Carolina, *J. geophys. Res.*, **87**, 6959–6974.

Zoback, M. D., Tsukahara, H. & Hickman, S., 1980. Stress measurements at depth in the vicinity of the San Andreas fault: implications for the magnitude of shear stress at depth, *J. geophys. Res.*, **85**, 6157–6173.

## Appendix A

The crack density $e(\xi)$ acts as a scaling parameter for the first-order correction terms to the elastic constants $\lambda_0$, $\mu_0$ of an intact isotropic medium. For elastic constants $A_{ij} \equiv C_{ij}/\rho$

expressed in units of km $s^{-2}$,

$$A_{ij}(\zeta) = A^0_{ij} + e(\zeta) A^1_{ij}, \tag{A1}$$

where, as in Hudson (1981), Červený & Pšenčík (1972) and Crampin (1984), $A_{ij}$ abbreviates the symmetrized elastic four-index tensor $C_{ijk}$ as $A_{ij} = 0$ except for

$$A_{ij} \leftrightarrow C_{iijj/\rho} \qquad i, j = 1, 2, 3$$

and

$$A_{kk} \leftrightarrow C_{ijij/\rho} \qquad i, j = 1, 2, 3 \quad k = 9 - i - j.$$

Our elastic tensors $A^0_{ij}$ and $A^1_{ij}$ are explicitly,

$$A^0_{ij} = \begin{bmatrix} \lambda+2\mu & \lambda & \lambda & & & \\ \lambda & \lambda+2\mu & \lambda & & 0 & \\ \lambda & \lambda & \lambda+2\mu & & & \\ & & & \mu & & \\ & 0 & & & \mu & \\ & & & & & \mu \end{bmatrix} \tag{A2}$$

$$A^1_{ij} = \frac{1}{\mu} \begin{bmatrix} \lambda^2 & \lambda^2 & \lambda(\lambda+2\mu) & & & \\ \lambda^2 & \lambda^2 & \lambda(\lambda+2\mu) & & 0 & \\ \lambda(\lambda+2\mu) & \lambda(\lambda+2\mu) & (\lambda+2\mu)^2 & & & \\ & & & 2\mu^2 & & 0 \\ & 0 & & & 2\mu^2 & \\ & & & 0 & & 0 \end{bmatrix} \begin{bmatrix} U_{33} & & & & & \\ & U_{33} & & & & 0 \\ & & U_{33} & & & \\ & & & U_{11} & & \\ & 0 & & & U_{11} & \\ & & & & & U_{11} \end{bmatrix}$$

where $U_{11} = 16/3\ (\lambda + 2\mu)/(3\lambda + 4\mu)$ and $U_{33} = 4/3\ (\lambda + 2\mu)/(\lambda + \mu)$.

## Appendix B

The Červený method of characteristics (Červený 1972; Červený & Pšenčík 1972; Červený & Firbas 1984) expresses the geometric ray approximate solution to the wave equation for a 2-D inhomogeneous, anisotropic medium as a pair of systems of coupled first order non-linear differential equations (Červený & Pšenčík 1972). For the $P$–$SV$ ray system in coordinates $(x, z)$, elastic constants $A_{ij}$ given in Appendix A, ray vector $(p, q)$, and wavefront time parameter $\tau$,

$$\frac{dx}{d\tau} = p\,(A_{11} + A_{55} - 2A_{11}A_{55}p^2 + Aq^2)/D$$

$$\frac{dz}{d\tau} = q\,(A_{33} + A_{55} - 2A_{33}A_{55}q^2 + Ap^2)/D$$

$$\frac{dp}{d\tau} = -\,[A_{11x}p^2D_2 + A_{33x}q^2D_1 + A_{55x}F + 2A_{13x}p^2q^2(A_{13} + A_{55})]/2D$$

$$\frac{dq}{d\tau} = -\,[A_{11z}p^2D^2 + A_{33z}q^2D_1 + A_{55z}F + 2A_{13z}p^2q^2(A_{13} + A_{55})]/2D$$

$$A_{ijx} = \partial_x A_{ij}, \quad A_{ijz} = \partial_z A_{ij}, \quad D = D_1 + D_2$$

$$D_1 = 1 - A_{11}p^2 - A_{55}q^2, \quad D_2 = 1 - A_{55}p^2 - A_{33}q^2$$

$$A = A_{13}^2 + 2A_{13}A_{55} - A_{11}A_{33}$$

$$F = p^2 + q^2 - A_{11}p^4 - A_{33}q^4 + 2p^2q^2A_{13}.$$

For the *SH* system, which in a 2-D medium decouples from the *P–SV* system,

$$\frac{dx}{d\tau} = pA_{66}$$

$$\frac{dz}{d\tau} = qA_{44}$$

$$\frac{dP}{d\tau} = -\tfrac{1}{2}(A_{66x}p^2 + A_{44x}q^2)$$

$$\frac{dq}{d\tau} = -\tfrac{1}{2}(A_{66z}p^2 + A_{44z}q^2),$$

where the elastic constants $A_{ij}$, $A_{ijx}$ and $A_{ijz}$ are designated above and $(p, q)$ is the ray vector. The four-fold and two-fold system of equations may be integrated by a Runge–Kutta procedure (e.g. Beyer 1984) provided initial conditions are known. The components of the initial ray vector $(p_0, q_0)$ are not independent. We may, however, specify a ray angle $\phi_0$ and evaluate the initial *P*, *SV* or *SH* velocity (Červený & Pšenčík, 1972): $p_0 = \cos\phi/V_p(x_0, z_0)$, $p_0 = \cos\phi_0/V_{SV}(x_0, z_0)$ or $p_0 = \cos\phi_0/V_{SH}(x_0, z_0)$ and $q_0 = \tan\phi_0 p_0$.

## Appendix C

The accuracy of the computed travel times and travel paths depends on three considerations. Theoretically, the first-order ray expansion given by Červený (1972) is valid only for wave frequencies that exceed the velocity gradients of the model medium. Second, the fracture density parameter $e(\zeta)$ has meaning only if the fractures are non-interacting, i.e. only if each fracture appears isolated in an otherwise homogeneous isotropic medium. Third, the Runge–Kutta integration procedure must be sufficiently fine in step size and of sufficiently high order to produce consistently accurate estimates of higher order derivatives. Having achieved a stable, physically plausible fit to the observed travel times and, where testable, travel paths, we now verify the three criteria for stable application of ray theory to a fractured medium.

### (i) THE HIGH-FREQUENCY APPROXIMATION

The fundamental frequencies of the seismic waves observed at Oroville lie between 30 and 50 Hz for *P*-waves and between 10 and 30 Hz for shear-waves. The minimum radial frequency $\omega$ is for *P*-waves is $2\pi \cdot 30 \simeq 200\ \mathrm{rad\,s^{-1}}$; for shear-waves, $\omega \simeq 2\pi \cdot 10\ \mathrm{Hz} = 60\ \mathrm{rad\,s^{-1}}$. From Fig. 9, the *P*-wave velocity gradient of the model medium for the vicinity of the Cleveland Hill fault has a maximum value of $(1\ \mathrm{km\,s^{-1}})/20\ \mathrm{m} \sim 50\ \mathrm{s^{-1}}$; for shear-waves the maximum velocity gradient is about $5\ \mathrm{s^{-1}} \ll 60\ \mathrm{s^{-1}}$. These gradients are at the limit of validity. However, the velocity gradients are maximum in a limited zone at the transition between the fault and the foot wall; elsewhere the velocity gradients are comfortably below the frequency limits.

(ii) THE DILUTE FRACTURE APPROXIMATION

The model fracture density distribution peaks in the range of 0.06–0.08 in the hanging wall. The definition of $e(\zeta)$ in terms of fractures per unit volume is

$$e \equiv Na^3/V,$$

where $a$ is the radius of a flat circular fracture ellipsoid, $N$ is the number density of fractures and $V$ is a unit volume. Fractures may be thought of as non-interacting if for a number density $N = 1$ a given value of $\epsilon$ results in a crack of radius small in comparison to the side $b$ of a cubic volume. For $\epsilon$ in the range of 0.06–0.08, $a/b \sim 0.40$–0.45. This ratio begins to violate the dilute approximation of Hudson (1981). The model fracture density in the vicinity of the fault is likely to be quantitatively inexact. However, it is clear that fracture density increases markedly as the fault zone is approached.

(iii) CONTROLS FOR NUMERICAL ACCURACY

Two such controls may be applied. First, Červený & Pšenčik (1972) provide an independent invariant relationship between wavenumber components $(p, q)$ which must be satisfied at each step in the computation. We monitored the relationship, finding it to be obeyed to a nominal 1–10 ppm and a worst case accuracy of 1000 ppm. The second check on computational stability is to vary the step size and/or order of the Runge–Kutta algorithm (Beyer 1984). The step size was checked occasionally. At no time did doubling the step size significantly deteriorate the computation nor did halving the step size change the travel time or travel path. A 4th-order Runge–Kutta algorithm was used throughout and was marginally different from a 3rd-order algorithm. We conclude that our computations are numerically accurate.